

Giacomo Franceschetto franceschettogcm@gmail.com

# Neutron Spectroscopy and phonon background estimation of MOF-based Room-Temperature Magnets

05/09/2021 - 02/10/2021

## CONTENTS

<b>Introduction</b>	<b>2</b>
<b>1 Experimental setup</b>	<b>2</b>
1.1 Samples . . . . .	2
1.2 Instrument . . . . .	4
<b>2 Modelling</b>	<b>5</b>
<b>3 Data collection</b>	<b>6</b>
3.1 Experimental Logbook . . . . .	6
3.2 Raw data . . . . .	6
<b>4 Data analysis</b>	<b>7</b>
4.1 Empty can background subtraction . . . . .	8
4.2 Phonon background estimation . . . . .	8
4.2.1 Q dependence . . . . .	8
4.2.2 E dependence . . . . .	9
4.2.3 Simulated phonon map . . . . .	9
4.2.4 Correctness check . . . . .	10
4.3 Subtraction . . . . .	11
<b>5 Results</b>	<b>11</b>
<b>6 Conclusions</b>	<b>12</b>
<b>Bibliography</b>	<b>14</b>
<b>Appendix: Complete results</b>	<b>15</b>

## INTRODUCTION

Magnets are an integral part of our everyday lives, they serve as critical components of the speakers in nearly all electronic devices, of medical devices [1], and of the information-storage media in computers[2]. Despite this importance, progress in developing new permanent magnets with improved properties has stagnated. Many of such materials are composed of metallic elements or rare earth; they can be expensive to fabricate and access to their constituent elements is often limited[3].

These limitations have motivated researchers to try to fabricate high-performance magnets at low energy and financial cost using molecular units of abundant metal ions and inexpensive organic ligands[3]. In principle, the right choice of metal ion and linker can give materials with programmed structures and magnetic properties. Moreover, the use of radicals can provide strong magnetic coupling between spin centres, a key feature for high-temperature magnetic order[2].

In recent years it is emerging a new strategy to design magnets based on coordination networks composed of anionic organic linkers and paramagnetic metal ions, metal-organic frameworks (MOFs). Framework design permits a remarkable degree of synthetic control and its lightweight, highly porous structure enables their use in a wide range of applications [3]. Furthermore, the process of synthesizing these magnets is relatively straightforward and applicable to different building blocks.

During my work at ILL, we investigated the magnetic properties of MOF based magnets through the technique of neutron spectroscopy. Inelastic neutron scattering is by far the most important tool to investigate dynamic correlations in condensed matter [4]. In fact, neutrons allow a sizeable momentum transfer at energy scales valid for collective excitations like phonons and magnons.

In this report, I start describing the two MOFs samples considered in the analyses and presenting previously published data of one of these samples. Section 2 is about Panther, the ILL instrument used in this experiment, and the next ones discuss data collecting, analysis, and the final results.

## 1 EXPERIMENTAL SETUP

### 1.1 Samples

The two samples whose magnetic properties we investigated are recently discovered metal-organic magnets. Both compounds are based on two-dimensional coordination networks of Chromium Cr and pyrazine pz, alternated by layers of Chloride and Lithium for the first sample,  $\text{Cr}(\text{pz})_2 \cdot 0.7\text{LiCl}$  (*I sample*), and by layers of Iodide and Lithium for the second sample,  $\text{Cr}(\text{pz})_2 \cdot \text{XLiI}$  (*II sample*). These two crystalline framework materials are very similar, hence we expect similar behaviours.

We can describe more in depth the *I sample* as it was studied in previous works [2]. This compound was synthesized starting from the reaction of  $\text{CrCl}_2$  with pyrazine,

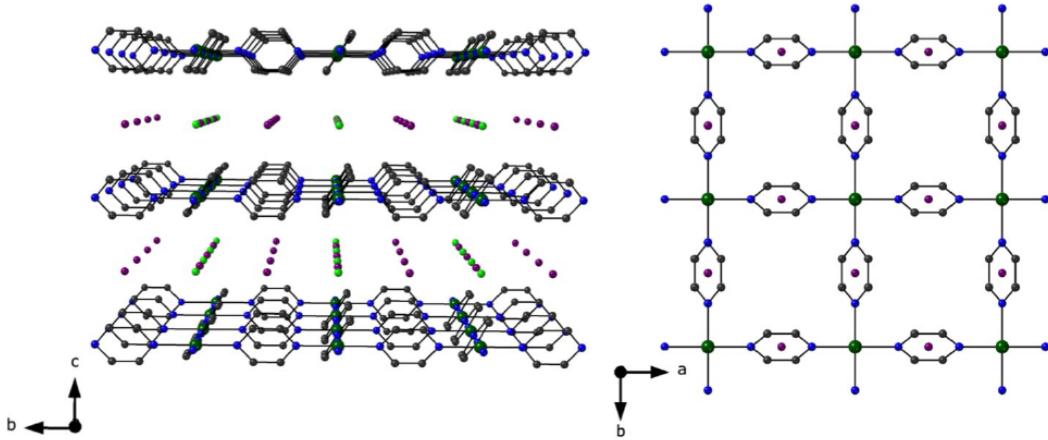
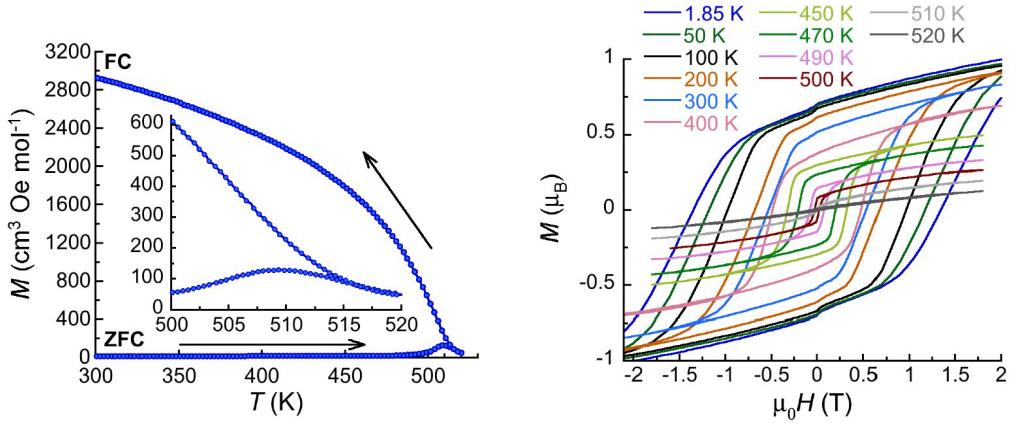


**Figure 1:** Structural model of  $\text{Li}_{0.7}[\text{Cr}(\text{pyz})_2]\text{Cl}_{0.7} \cdot 0.25(\text{THF})$ , Cr: dark green, N: blue, C: black, Cl: light green, Li: purple. [2]

then a chemical reduction was performed giving a material containing two-dimensional sheets of square planar  $S = 2 \text{ Cr}^{\text{II}}$  centers linked by pz radical anions (Figure 1). The magnetic properties of *I sample* were studied through a vibrating sample magnetometer capable of achieving temperatures up to 600K. Zero-field cooled (ZFC)/field-cooled (FC) magnetization data were collected under a *dc* field of 50 Oe showing that the magnetization bifurcation point, which corresponds to the temperature at which the coercive field vanished, is around 510 K (Figure 2 (a)). At a similar temperature the magnetic hysteresis,  $M$  vs  $H$ , curves (Figure 2 (b)) close reaching a linear dependence, so we can expect the critical temperature to be near that value.



(a) Zero field-cooled (ZFC)/field-cooled (FC) magnetization data      (b) Magnetization versus applied dc magnetic field data

**Figure 2:** Magnetic properties of *I sample* [2]

## 1.2 Instrument

Panther is a thermal neutron Time Of Flight (TOF) spectrometer installed on the H12 thermal beam tube in the reactor hall and designed for measurements of excitations in condensed matter [5]. A detailed instrument layout is still not available for this instrument because Panther was recently built as an update of the previous IN4C, another TOF spectrometer. Hence, we can use the IN4C layout to better describe the TOF technique.

Looking at the Figure 3 (a) we notice how the neutron beam is first optimized by two background choppers and then the incoming energy is determined by a monochromator. Before reaching the sample, neutrons encounter a straight slit Fermi chopper that produces short pulses. Lastly, neutron bunches are collected by the detector. The selection of the neutrons from the beam is represented in the scheme in Figure 3 (b).

Having the time of flight between the chopper and the detector and the angle between the incident and scattered neutron wavevectors, the energy transfer and the scattering vector  $Q = k_i - k_f$  can be obtained [6]. The basic quantities measured by TOF instruments are a series of intensities for specific angles and time channels. Angles and time can be themselves converted into momentum and energy transfers.

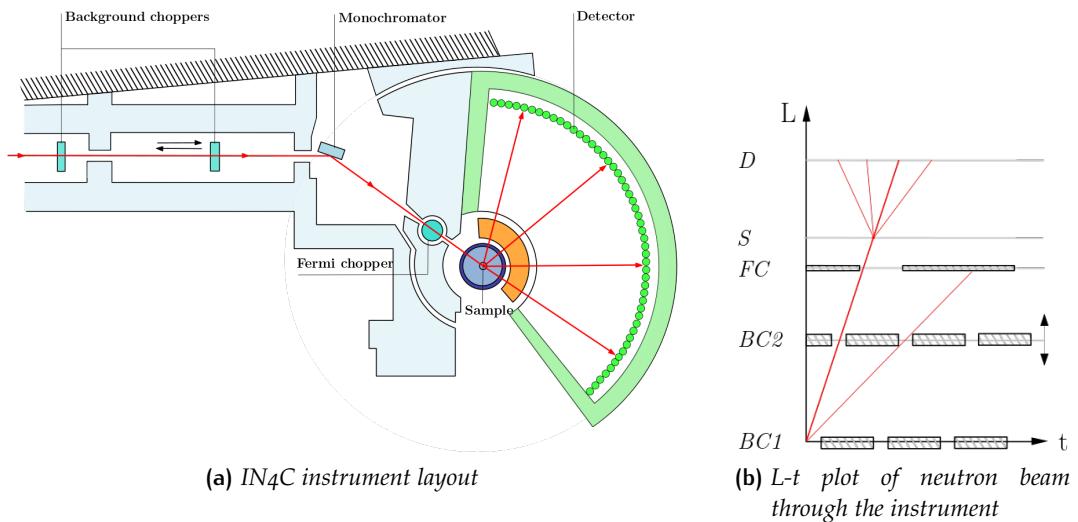
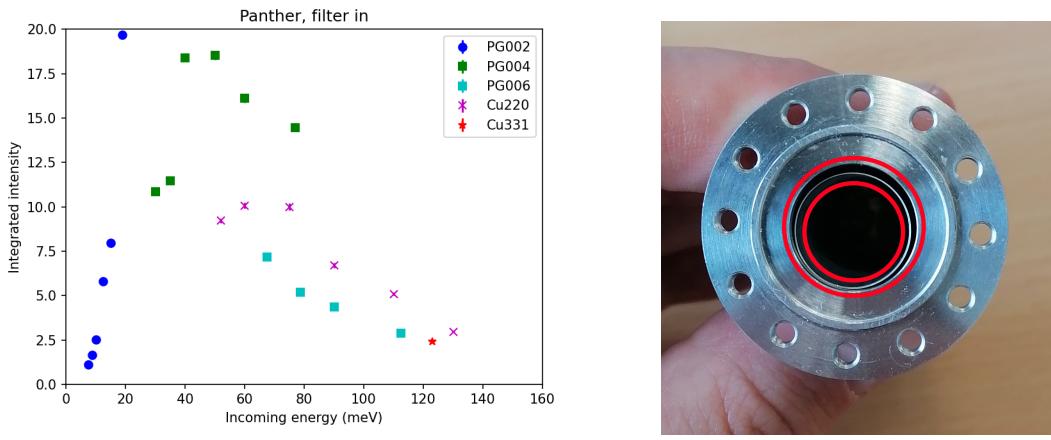


Figure 3: Time of Flight technique

Panther is optimized for energy transfers in the range 2 – 60 meV and it can reach up to 150 meV. We observe how the integrated intensity from a vanadium sample (incoherent scatterer used for normalization and calibration) varies at different incoming energies and depends on the monochromator. For example, for the Pyrolytic Graphite (PG) 002 Bragg reflection (blue points on Figure 2 (a)), it reaches the maximum around 20 meV.



(a) Integrated intensity vs incoming energy for neutrons scattered from vanadium sample at Panther

(b) Aluminium sample cans

Figure 4: Instrument details

During the experiment, the compounds were put inside aluminium sample cans, precisely inside the area between the can and the inside cylinder, as highlighted in Figure 4 (b). These cans are almost transparent to neutrons, and the thin layer of sample is meant to avoid noise due to multiple scattering<sup>1</sup>.

## 2 MODELLING

The magnetic excitations expected for *I sample* were calculated thanks to SpinW [7], a Matlab library that numerically simulates magnetic dynamics given a certain structure. The result is shown in Figure 5.

Two horizontal bands of higher intensity, corresponding to collective magnetic excitations, magnons, are present at 55 and 150 meV. Usually, we would expect the intensity of the bands to decrease with the increasing of the momentum transfer, having no persistence of the magnetic signal above  $6 \text{ \AA}^{-1}$ . Instead, in this plot we observe a constant scattering intensity along the scattering momentum axis. This is due to the magnetic form factor of the compound not taken into account in the calculation. The reason behind that relies on the fact that half of the spin centers are radical ligands, pyrazine, which does not have a well-defined form factor. Consequently, the form factor was completely omitted due to avoid bias in the calculation.

Therefore, in our experiment we expect to detect the 55 meV horizontal band but only for low  $Q_s$  since the higher energy band is out of range for Panther.

---

<sup>1</sup>Multiple scattering happens when a neutron scatters from the sample more than once. In that case, it changes momentum (and maybe energy) twice, and we have no way of knowing the initial conditions that caused the scattering in the first place.

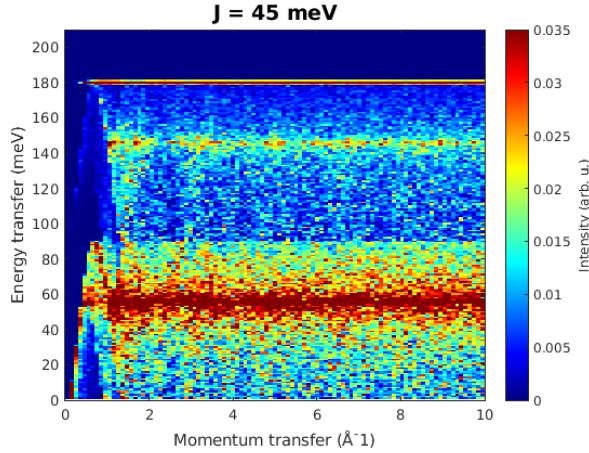


**Figure 5:** SpinW modeling of the *I* sample

### 3 DATA COLLECTION

#### 3.1 Experimental Logbook

In Table 1, we listed the measurements performed on the two samples. For most of them the temperature was fixed at 1.6 K with the aim of minimizing the noise, then few runs were made at 100 K. Due to the high ordering temperature we do not expect anything to be different changing the sample temperature. These measurements were driven by the fact that we had tried everything else obtaining no results matching the expectations and persisting on the same conditions was pointless. Different incoming energies were selected from 19 meV, for which we have the maximum intensity of the beam, to the highest incoming energy reachable by Panther, 150 meV. These runs were performed during two full days of beamtime [8].

Run	Temperature (K)	Incoming energy (meV)	Sample
1	1.6	76	I
2	1.6	112	I
3	1.6	19	I
4	1.6	150	I
5	1.6	76	II
6	1.6	112	II
7	1.6	19	II
8	1.6	150	II
9	100	76	I
10	100	150	I

**Table 1:** Logbook

#### 3.2 Raw data

Collected data can be represented as two-dimensional plots with the momentum  $Q$  and energy  $E$  transfers in the axes and the scattering intensity through a colormap. In

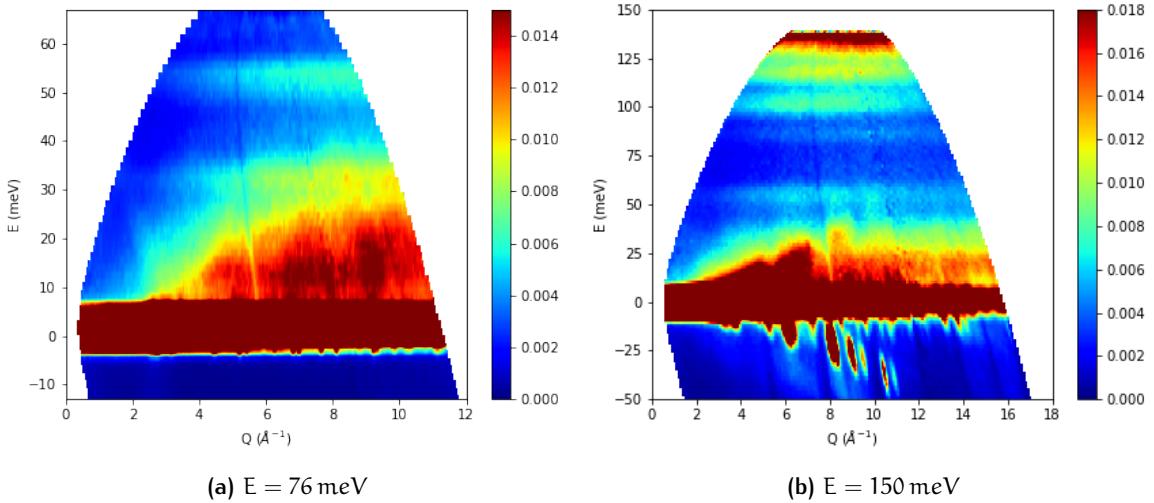


**Figure 6:** Raw data collected at  $T = 1.6$  K for  $I$  sample

Figure 6 (a), (b) we reported raw data of  $I_{sample}$  measured at  $T = 1.6$  K for incoming energies of 76 meV and 150 meV.

For both incoming energies we can notice that there is no high intensity horizontal band decreasing with  $Q$  as one would expect for magnetic excitations. Otherwise, we can distinguish horizontal bands whose intensity is increasing along the momentum transfer axis. This behavior is typical of phonons[9] as we can observe looking at the phonon differential scattering cross section [10]:

$$\frac{d^2\sigma_{ph}}{dEd\Omega} \propto e^{-2W(Q)} \sum_s \frac{(\mathbf{Q} \cdot \mathbf{e}_s)^2}{2M\omega_{q_s}} \quad (1)$$

where  $\mathbf{Q}$  is the scattering vector,  $W(\mathbf{Q})$  stands for the Debye-Waller factor,  $\mathbf{e}_s$  and  $\omega_{\mathbf{q}_s}$  are the vibrational eigenvector and frequency of the specific phonon mode  $s$ , and  $M$  is the mass of each nucleus.

For different incoming energies and for *II sample* we obtained similar results ([Appendix](#)).

## 4 DATA ANALYSIS

In Figure 6 (a), (b), we can distinguish horizontal bands at 33, 55, 85, 102 and 120 meV. All these increase in intensity with increasing  $Q$ , meaning they are vibrational modes and not of magnetic origin. Moreover, the fact that they are dispersionless, their energy does not depend on  $Q$ , tell us that they are probably vibrational eigenmodes on individual molecules. Hence, since from the collected data we do not see a clear evidence of magnetic excitations contribution to the scattering intensity, the analysis has been focused on trying to isolate and subtract from the raw data the scattering contribution due to the phonons. We performed this kind of analysis for every run

of collected data, in this report we are going to focus particularly on the run taken at  $E = 76 \text{ meV}$ ,  $T = 1.6 \text{ K}$  for *I sample*.

#### 4.1 Empty can background subtraction

First step to eliminate some noise is to subtract from the raw data the scattering intensity due to the empty can, this was done only for Runs: 1, 3, 5, 7 (Tab. 1). At this conditions of temperature and incoming energy, a previous measurement was taken without the sample inside the aluminium can. We used these data to perform a first subtraction (Figure 7).

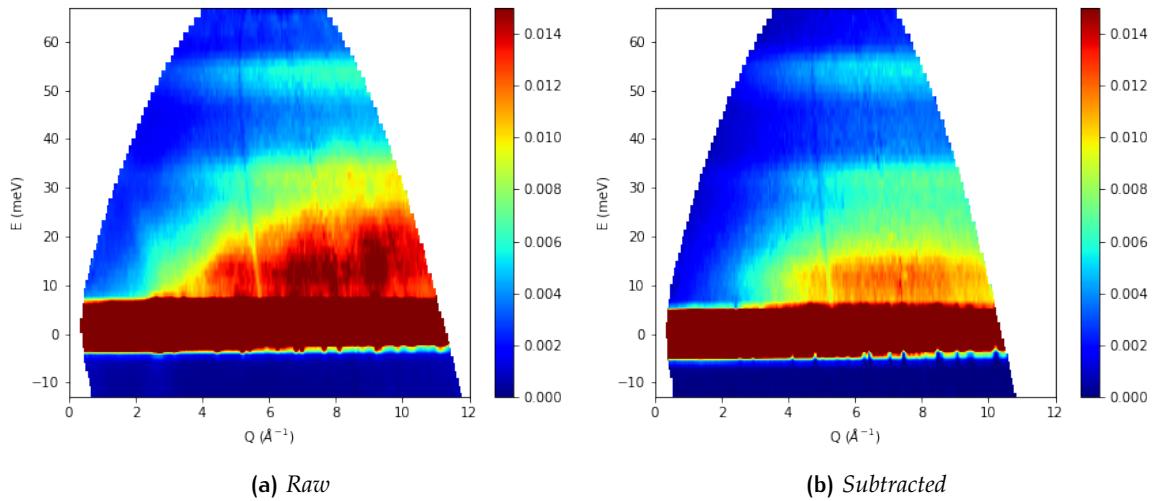


Figure 7: Empty can subtraction for  $E = 76 \text{ meV}$ ,  $T = 1.6 \text{ K}$ , *I sample*

#### 4.2 Phonon background estimation

One method to compute the simulated phonon map consists in detecting a specific dependence of the phonon scattering intensity for both  $Q$  and  $E$ .

##### 4.2.1 $Q$ dependence

For the momentum transfer, we focused on the three higher intensity horizontal bands at 10, 35 and 55 meV (Figure 7 (b)). Recalling equation (1), we can model the phonon scattering intensity at fixed energy  $E^*$  with a rough approximation:

$$S(Q, E^*) = a + bQ^2 e^{-cQ^2} \quad (2)$$

where  $a$ ,  $b$ ,  $c$ , are real parameters and  $Q$  is the module of the scattering vector. Thanks to Equation 2, we fitted the  $Q$  dependences at the three different energies (Figure 8). In the fitting process only part of the data was used, as it is evident in the residuals plots.

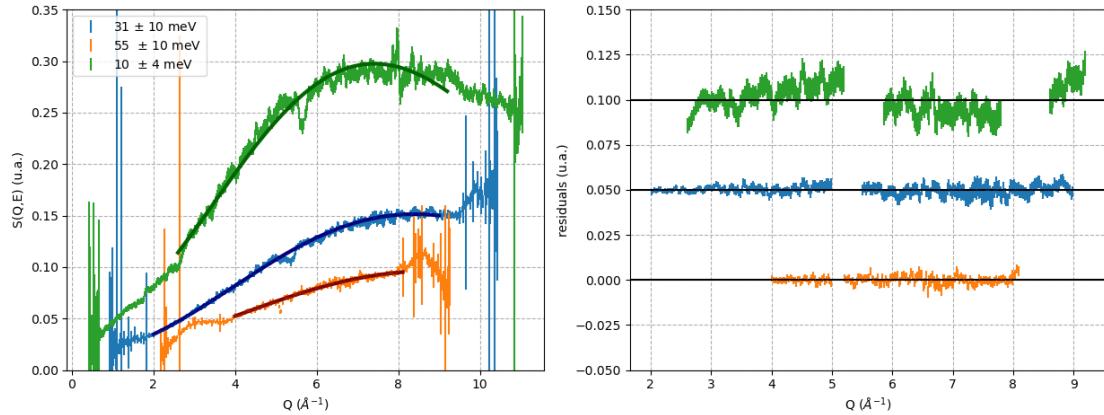


**Figure 8:** Q dependences for  $E = 76$  meV,  $I$  sample

It is clear that Equation 2 actually describes the data solidly. However, the phonon modes are well isolated, and it turns out that their individual Q-dependence is quite different, which, given Equation 1, means that their vibrational eigenvectors,  $\mathbf{e}_s$ , are different. As a first approximation, we can take the 10 meV cut to calculate the phonon map. In principle, choosing a single Q-dependence is wrong since we measure three different ones, but our method works if we have exactly one Q-dependence. The choice of the 10 meV cut is justified by the fact that this horizontal band is not defined as well as the others. So, if we are sure that the 35 and 55 meV cuts correspond to specific phonon modes, it might be that the 10 meV one is the outcome of various modes, indeed more general.

#### 4.2.2 $E$ dependence

Thereafter we selected a Q value for which we do not expect any scattering intensity due to magnetic excitations, thus  $Q > 6/\text{Å}\text{\AA}^{-1}$  as mentioned earlier, and extracted the energy dependence. In this case we integrated for  $Q = 7 \pm 0.8 \text{ Å}^{-1}$  (Figure 9).

It is important to mention that the outcoming energy dependence also corresponds to the neutron-weighted density of states.

#### 4.2.3 Simulated phonon map

Having energy and momentum transfer dependences, we can compute the simulated phonon map  $S_{\text{ph}}(Q, E)$ . Firstly, it is necessary to normalize the Q dependence such that its intensity for the Q value at which we extracted the E dependence is 1:

$$\overline{S(Q, 10 \text{ meV})} = \frac{S(Q, 10 \text{ meV})}{S(7 \text{ Å}^{-1}, 10 \text{ meV})} \quad (3)$$

Then, it is possible to compute every E dependence at a certain  $Q^*$  simply by taking the selected weighted density of states at  $Q = 7 \text{ Å}^{-1}$  and scaling it by the normalized intensity  $\overline{S(Q^*, 10 \text{ meV})}$ .

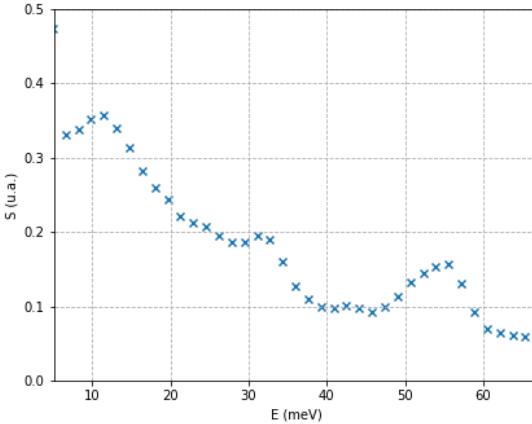
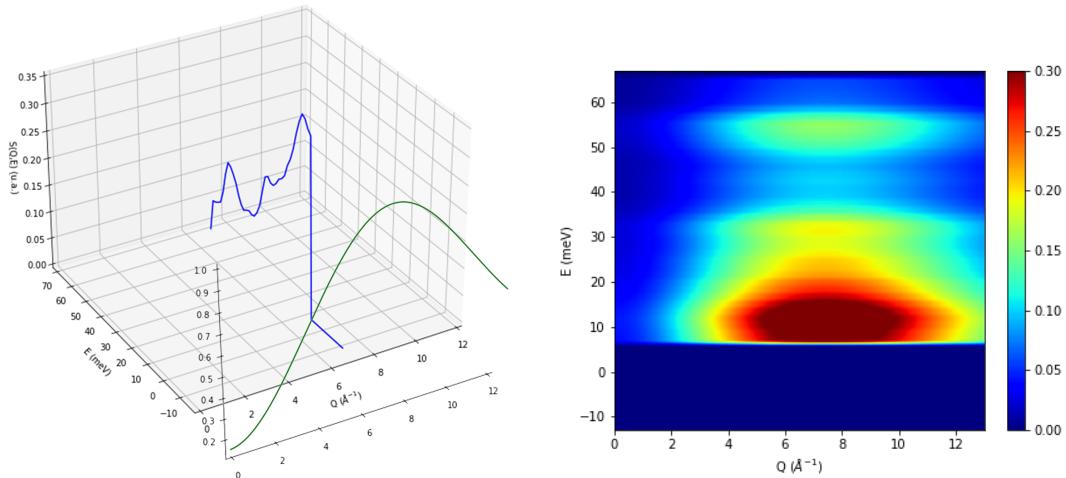


**Figure 9:** E dependence at  $Q = 7 \pm 0.8 \text{ \AA}^{-1}$  for  $E = 76 \text{ meV}$ ,  $T = 1.6 \text{ K}$ , *I sample*



**(a)** 3D view of E dependence at  $Q = 7 \text{ \AA}^{-1}$  and of normalized Q dependence at  $E = 10 \text{ meV}$  **(b)** Simulated phonon map for  $E = 76 \text{ meV}$ ,  $T = 1.6 \text{ K}$ , *I sample*

**Figure 10:** Computing of the simulated phonon map

In the Figure 10 (a), we represented the two dependences selected to generate the phonon map reported in Figure 10 (b).

#### 4.2.4 Correctness check

We also performed a correctness check of the simulated phonon map comparing energy dependences at various Qs for both raw data and phonon map. For  $Q = 7 \text{ \AA}^{-1}$  the dependences are the same. Instead, for different Qs, the two weighted densities of states slightly differ (Figure 11). This behaviour matches the expectation, in fact in the first case we are focusing on the same momentum transfer used for generating the entire phonon map, so it is correct to obtain the same pattern. Whereas, for different Q values the two energy distributions differ as it is expected. As we are doing a crude approximation we would not be surprised to see even bigger differences between

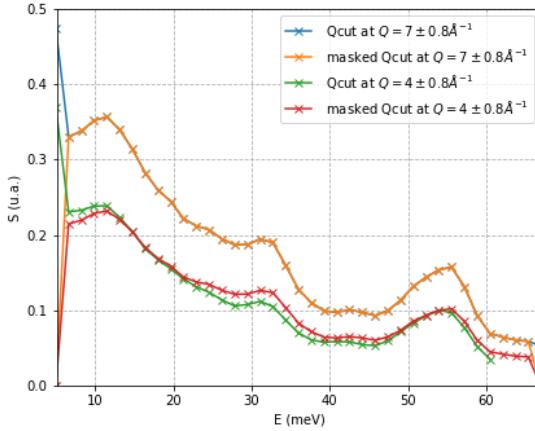


**Figure 11:** Correctness check of the simulated phonon map for  $E = 76$  meV,  $T = 1.6$  K,  $I_{\text{sample}}$

model and data at  $Q = 4 \text{ \AA}^{-1}$ . Therefore, the fact that the differences are little gives us confidence about the simulated phonon map.

#### 4.3 Subtraction

Once obtained the simulated phonon map, we must scale it before subtracting it from the raw data. As a matter of fact, we generated the phonon distribution starting from integrated cuts, so the intensities obtained at fixed  $Q$  contain the contribution due to more than one point of the initial raw data map. Consequently, we performed a normalization looking at the ratio  $r$  between the integrated intensities of a  $Q \pm \delta Q$  cut and those of single  $Q$  value. The normalized phonon map would be:

$$\overline{S_{\text{ph}}(Q, E)} = \frac{S_{\text{ph}}(Q, E)}{r} \quad (4)$$

Then we can compute the subtracted map (Figure 12 (b)):

$$S_{\text{sub}}(Q, E) = S_{\text{raw}}(Q, E) - \overline{S_{\text{ph}}(Q, E)} \quad (5)$$

## 5 RESULTS

Looking at the final results, we first observe that the phonon bands have been well subtracted. However, it is evident how there is a trend of over-subtracting for low values of  $Q$  and under-subtracting for high values of  $Q$ . This is probably due to the crude approximation done in selecting only one  $Q$  dependence for simulating the phonon map.

Furthermore, we can notice an higher intensity horizontal band around the same energy value for which we expected a magnetic excitation from the modeling. This region is highlighted with a red circle in Figure 13.

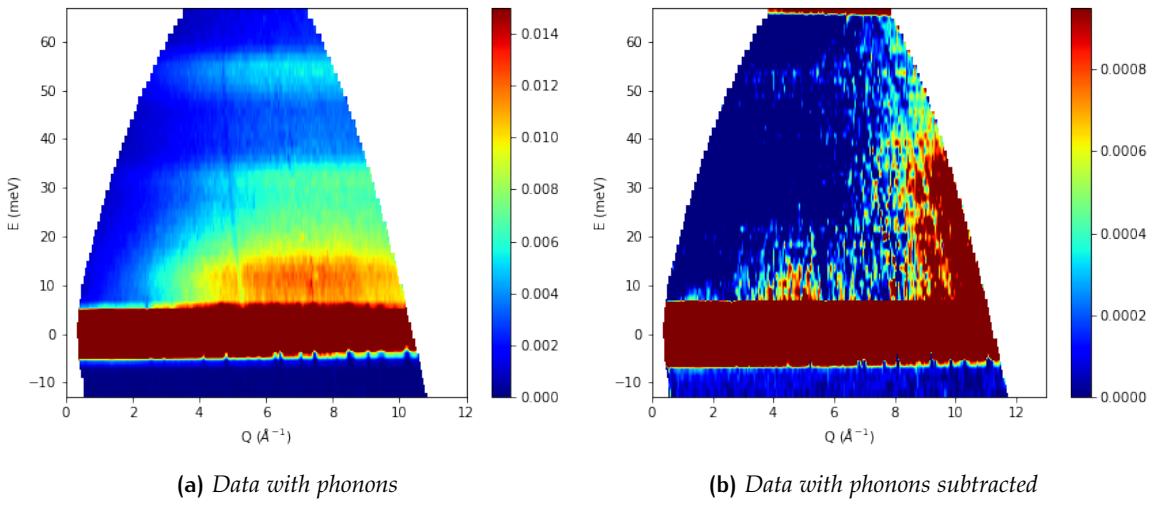


**Figure 12:** Subtraction process for  $E = 76 \text{ meV}$ ,  $T = 1.6 \text{ K}$ ,  $I_{\text{sample}}$

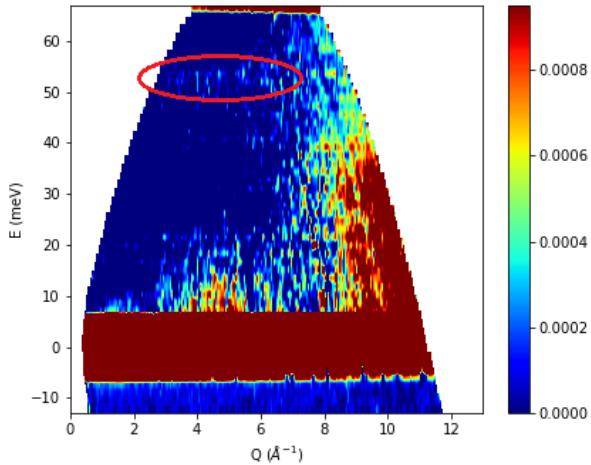


Figure 13: Data with phonons subtracted for  $E = 76$  meV,  $T = 1.6$  K,  $I$  sample

## 6 CONCLUSIONS

This work wanted to achieve measurements of magnetic excitations on *I, II sample* through inelastic neutron scattering. After a brief description of the analyzed sample and of the instrument used, we presented the measurements performed during the two days of beamtime at ILL. Then, due to experimental results different from the modelling expectations, the focus of the analysis moved on a first approximation simulation of the phonon map. In fact, in our data, we could not detect any magnetic excitation but only phonons contribution to the scattering intensity. Therefore, we subtracted the simulated phonon maps to the raw data obtaining slight evidence of intensity in a region matching

the modelling.

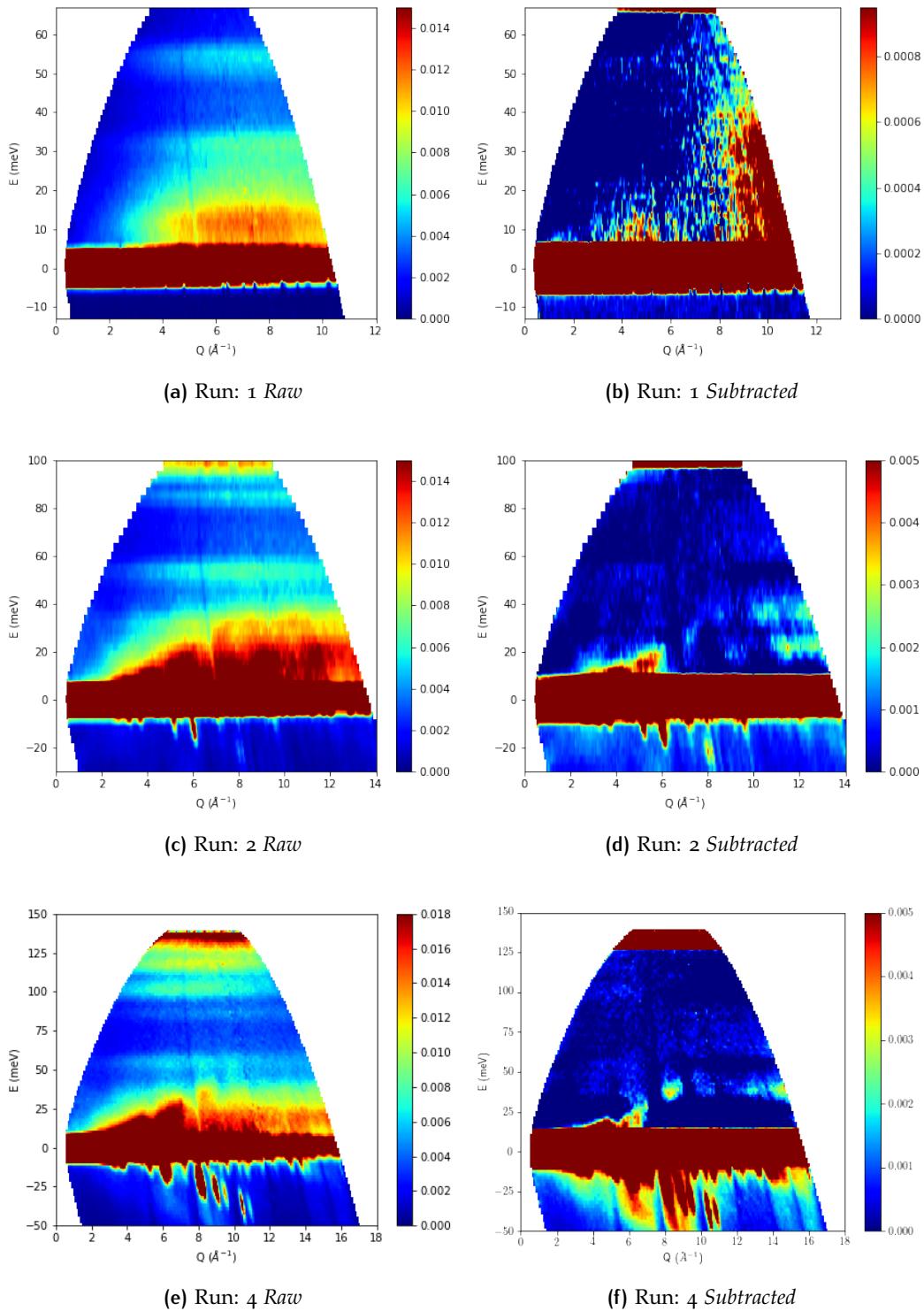
Despite that, the intensity of this band is very low, and it clearly does not allow us to state that we found the magnetic excitations expected from the model. However, it is for sure a good starting point for further investigations. For instance, thanks to DFT calculations, a more accurate phonon map can be developed considering specific Q dependences for specific energies.

## BIBLIOGRAPHY

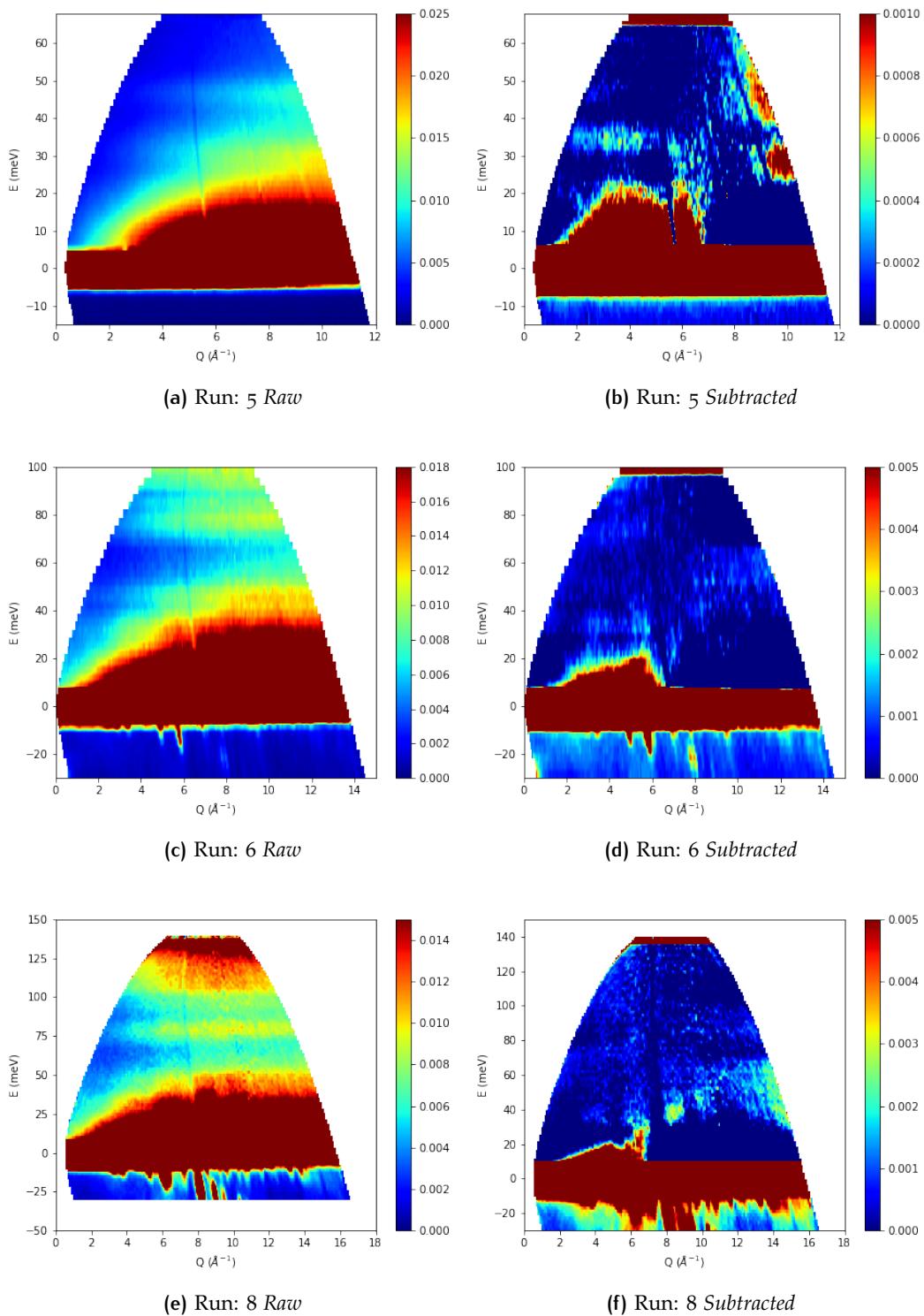
- [1] *Scientists design magnets with outstanding properties - new lightweight magnets have possible real-world applications*, Nov. 2020. [Online]. Available: <https://www.jyu.fi/en/current/archive/2020/11/scientists-design-magnets-with-outstanding-properties-new-lightweight-magnets-have-possible-real-world-applications>.
- [2] P. Perlepe, I. Oyarzabal, A. Mailman, M. Yquel, M. Platunov, I. Dovgaliuk, M. Rouzières, P. Négrier, D. Mondieig, E. A. Suturina, and et al., "Metal-organic magnets with large coercivity and ordering temperatures up to 242°C," *Science*, vol. 370, no. 6516, pp. 587–592, 2020. DOI: [10.1126/science.abb3861](https://doi.org/10.1126/science.abb3861).
- [3] R. A. Murphy, J. R. Long, and T. D. Harris, "A hard permanent magnet through molecular design," *Communications Chemistry*, vol. 4, no. 1, 2021. DOI: [10.1038/s42004-021-00509-y](https://doi.org/10.1038/s42004-021-00509-y).
- [4] P. Mitchell, S. Parker, A. Ramirez-Cuesta, and J. Tomkinson, *Vibrational spectroscopy with neutrons: With applications in chemistry, Biology, Materials Science and Catalysis*. World Scientific, 2005.
- [5] [Online]. Available: <https://www.ill.eu/users/instruments/instruments-list/panther/description>.
- [6] J. R. Copley and T. J. Udovic, "Neutron time-of-flight spectroscopy," *Journal of Research of the National Institute of Standards and Technology*, vol. 98, no. 1, pp. 71–87, 1993. [Online]. Available: [https://www.ncbi.nlm.nih.gov/pmc/articles/PMC4927250/pdf/jresv98n1p71\\_a1b.pdf](https://www.ncbi.nlm.nih.gov/pmc/articles/PMC4927250/pdf/jresv98n1p71_a1b.pdf).
- [7] S. Toth and B. Lake, "Linear spin wave theory for single-q incommensurate magnetic structures," *Journal of Physics: Condensed Matter*, vol. 27, no. 16, p. 166002, 2015. DOI: [10.1088/0953-8984/27/16/166002](https://doi.org/10.1088/0953-8984/27/16/166002).
- [8] M. Baker, R. T. Christiansen, R. Clerac, B. Fak, G. Franceschetto, and J. Ollivier, "Magnetic excitations in high-*Tc* metal-organic magnets," *Institut Laue-Langevin (ILL)*, 2021. DOI: [doi:10.5291/ILL-DATA.4-06-19](https://doi.org/10.5291/ILL-DATA.4-06-19).
- [9] C. Kittel, "Introduction to solid state physics." Wiley, 1976, ch. 4, pp. 89–102.
- [10] I. A. Zaliznyak and J. M. Tranquada, "Neutron scattering and its application to strongly correlated systems," *Springer Series in Solid-State Sciences*, pp. 205–235, 2014. DOI: [10.1007/978-3-662-44133-6\\_7](https://doi.org/10.1007/978-3-662-44133-6_7).
- [11] K. S. Pedersen, P. Perlepe, M. L. Aubrey, D. N. Woodruff, S. E. Reyes-Lillo, A. Reinholdt, L. Voigt, Z. Li, K. Borup, M. Rouzières, and et al., "Formation of the layered conductive magnet  $\text{CrCl}_2(\text{pyrazine})_2$  through redox-active coordination chemistry," *Nature Chemistry*, vol. 10, no. 10, pp. 1056–1061, 2018. DOI: [10.1038/s41557-018-0107-7](https://doi.org/10.1038/s41557-018-0107-7).

## APPENDIX: COMPLETE RESULTS

In this appendix we report the subtractions performed for all the other datasets not described in this document.



**Figure 14:** *I sample*

**Figure 15:** II sample